

3 **PIFE-PIC: PARALLEL IMMERSED FINITE ELEMENT  
4 PARTICLE-IN-CELL FOR 3-D KINETIC SIMULATIONS OF  
5 PLASMA-MATERIAL INTERACTIONS\***

6 DAORU HAN<sup>†</sup>, XIAOMING HE<sup>‡</sup>, DAVID LUND<sup>†</sup>, AND XU ZHANG<sup>§</sup>

7 **Abstract.** This paper presents a recently developed particle simulation code package PIFE-PIC,  
8 which is a novel three-dimensional (3-D) parallel immersed finite element (IFE) particle-in-cell (PIC)  
9 simulation model for particle simulations of plasma-material interactions. This framework is based on  
10 the recently developed nonhomogeneous electrostatic IFE-PIC algorithm, which is designed to handle  
11 complex plasma-material interface conditions associated with irregular geometries using a Cartesian  
12 mesh-based PIC. Three-dimensional domain decomposition is utilized for both the electrostatic field  
13 solver with IFE and the particle operations in PIC to distribute the computation among multiple  
14 processors. A simulation of the orbital motion-limited (OML) sheath of a dielectric sphere immersed  
15 in a stationary plasma is carried out to validate parallel IFE-PIC and profile the parallel performance  
16 of the code package. Furthermore, a large-scale simulation of plasma charging at a lunar crater  
17 containing 2 million PIC cells (10 million FE/IFE cells) and about 1 billion particles, running for  
18 20,000 PIC steps in about 154 wall-clock hours, is presented to demonstrate the high-performance  
19 computing capability of PIFE-PIC.

20 **Key words.** immersed finite element, particle-in-cell, parallel domain decomposition, plasma-  
21 material interactions

22 **AMS subject classifications.** 35R05, 65N30, 65Y05

23 **DOI.** 10.1137/20M137344X

24 **1. Introduction.** Particle modeling of plasma dynamics has emerged as one of  
25 the most appropriate algorithms for first-principle-based modeling of many plasma-  
26 material interaction (PMI) problems. One of the fundamental phenomena in plasma-  
27 material interactions is surface charging. When an object is immersed in a plasma,  
28 its surface will collect charge from the plasma until it reaches an equilibrium sur-  
29 face potential determined by the current balance condition. Many plasma-material  
30 interaction problems involve multiple objects with complex geometries; therefore the  
31 interface conditions between the plasma and object need to be accurately resolved.

32 Being one of the most popular kinetic methods for collisionless plasma simulations,  
33 the particle-in-cell (PIC) method [11] models the charged particles as macroparticles  
34 and tracks the motions of particles in the electrostatic/electromagnetic field. The  
35 electric potential in a PIC simulation domain is governed by the second-order elliptic  
36 partial differential equations (PDEs) with discontinuous dielectric coefficients and

---

\*Submitted to the journal's Software and High-Performance Computing section October 14, 2020;  
accepted for publication (in revised form) February 22, 2021; published electronically DATE. Part of  
this work was previously presented as a conference paper in 2018 AIAA Aerospace Sciences Meeting  
(paper number AIAA 2018-2196) [37]. The work presented here has since been significantly revised  
and extended.

<https://doi.org/10.1137/20M137344X>

**Funding:** This work was partially supported by NASA Missouri Space Grant Consortium  
through NASA-EPSCoR-Missouri and by the NSF through grants DMS-2005272 and OAC-1919789.  
The third author was also supported in part by NASA-Missouri Space Grant Consortium Scholar-  
ships.

<sup>†</sup>Department of Mechanical and Aerospace Engineering, Missouri University of Science and Tech-  
nology, Rolla, MO 65409 USA (handao@mst.edu, dclgzb@mst.edu).

<sup>‡</sup>Department of Mathematics and Statistics, Missouri University of Science and Technology, Rolla,  
MO 65409 USA (hex@mst.edu).

<sup>§</sup>Department of Mathematics, Oklahoma State University, Stillwater, OK 74078 USA (xzhang@  
okstate.edu).

37 nonhomogeneous flux jumps across the material surface interface. Numerical methods  
 38 based on structured meshes, especially Cartesian meshes, are particularly desirable in  
 39 these simulations because they enable efficient particle tracking and save computing  
 40 time in PMIs.

41 The immersed finite element (IFE) method is a finite element method (FEM)  
 42 for solving interface problems using interface-independent meshes such as Cartesian  
 43 meshes [22, 24, 59, 61, 72, 78]. The main idea of IFE is to adjust approximating  
 44 functions locally to accommodate the physical interface conditions [12, 25, 42,  
 45, 43, 58, 60, 79]. An IFE method can achieve optimal convergence on an interface-  
 46 independent mesh with the number and location of the degrees-of-freedom isomor-  
 47 phic to the standard FEM on the same mesh [28, 29, 47, 62, 88]. The first IFE  
 48 method was introduced by Li in [59] for solving one-dimensional (1-D) elliptic inter-  
 49 face problems with piecewise linear polynomials. Since then, the IFE method has  
 50 been extended to higher-order approximations [2, 12, 14, 26, 31], various discretiza-  
 51 tion techniques [1, 4, 21, 44, 45, 48, 65], higher-dimensional elliptic interface problems  
 52 [27, 30, 41, 64, 78], and other interface PDE models [3, 7, 49, 63, 86, 87].

53 Over the past decade, the IFE method has been successfully used together with  
 54 PIC in plasma particle simulations [5, 6, 16, 17, 18, 81]. Recently, a nonhomogeneous  
 55 IFE-PIC algorithm has been developed for particle simulations of PMIs with complex  
 56 geometries while maintaining the computational speed of the Cartesian mesh-based  
 57 PIC [15, 40, 46, 66, 67]. To the best of our knowledge, most existing IFE-PIC algo-  
 58 rithms are serial. The nonparallel algorithms have limitations in their capability to  
 59 handle large-scale particle simulations and their efficiency in using multiple proces-  
 60 sors at the algorithm level. For a typical large-scale 3-D PIC simulation, millions to  
 61 billions of particles are tracked in the computation domain that contains millions of  
 62 elements. With the availability of multiprocessor computational facilities, the call for  
 63 parallel IFE-PIC algorithms is urgent.

64 The goal of this paper is to develop and test a new parallel IFE-PIC package for  
 65 particle simulations of electrostatic PMIs, namely, PIFE-PIC. We utilize a 3-D domain  
 66 decomposition technique for both *field-solve* and *particle-push* procedures of the PIC  
 67 model. The computations are distributed into multiple subdomains which can be han-  
 68 dled independently by multiple processors. The key is how to efficiently exchange the  
 69 information between these subdomains. In this work, neighboring subdomains have  
 70 a small overlapping (“guard cells”) region which will be used as a common region  
 71 to interchange the PDE solutions and the particle data. Extensive numerical exper-  
 72 iments show that our PIFE-PIC scheme significantly outperforms the serial IFE-PIC  
 73 scheme. Although it maintains a similar accuracy as the serial IFE-PIC computa-  
 74 tional scheme, the high parallel performance dramatically reduces the computational  
 75 time for problems of practical interests. Hence, large-scale kinetic simulations of PMIs  
 76 can be carried out much more efficiently.

77 The rest of this paper is organized as follows. In section 2, we describe the  
 78 details of 3-D domain decomposition for both IFE (field-solve) and PIC (particle-  
 79 push) procedures of PIFE-PIC. In section 3, we present a code validation using a  
 80 3-D sheath problem of a dielectric sphere immersed in a stationary plasma. Section  
 81 4 presents a parallel efficiency test of the PIFE-PIC code for strong scaling. Section  
 82 5 presents an application of PIFE-PIC to simulations of lunar surface charging at a  
 83 crater. Finally, a summary and conclusion are given in section 6.

## 84 2. PIFE-PIC algorithms.

85 **2.1. Overview of PIC and IFE-PIC.** PIC is a widely-used kinetic parti-  
 86 cle simulation method for plasma dynamics [11, 51]. In PIC, charged particles of

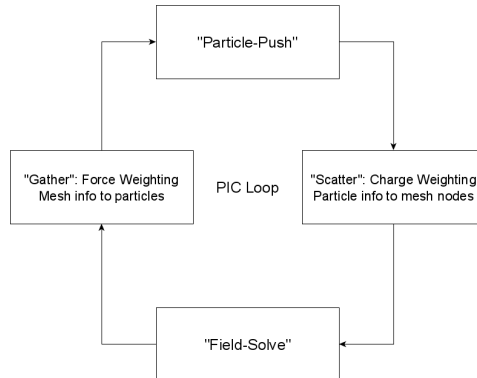
87 plasma species are represented by a number of simulation particles (also referred to  
 88 as macroparticles or superparticles) distributed “freely” in the entire computation  
 89 domain, while the field quantities such as electric potential are discretized on a mesh  
 90 (thus the name “particle-in-cell”). The kernel of PIC method is the “PIC loop” which  
 91 includes four essential steps: scatter, field-solve, gather, and particle-push (Figure  
 92 2.1). Within a PIC loop, quantities carried by the simulation particles are weighted  
 93 onto the mesh nodes (“scatter”) to form the right-hand side (RHS) term of the PDE  
 94 for the solution of the electrostatic/electromagnetic field (“field-solve”), which is in  
 95 turn interpolated at particle positions (“gather”) to update the velocity and position  
 96 of the particles (“particle-push”). Such data exchange between particles and field  
 97 quantities will iterate for a desired number of steps (or till a convergence criterion is  
 98 met) to obtain the self-consistent solution of both particles and fields.

101 For problems of PMIs, the mathematical model is an interface problem includ-  
 102 ing the electrostatic/electromagnetic field problem in a self-consistent solution to the  
 103 corresponding plasma dynamics problem (Figure 2.2(a)), together with the appropri-  
 104 ate interface conditions between the plasma region and the material region (Figure  
 105 2.2(b)). For electrostatic problems presented in this work, we consider the following  
 106 boundary value problem of the elliptic equation that governs the distribution of the  
 107 electric potential  $\phi$  [52]:

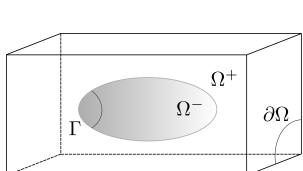
$$108 \quad (2.1) \quad -\nabla \cdot (\varepsilon \nabla \phi(X)) = \rho(X), \quad X = (x, y, z) \in \Omega^- \cup \Omega^+,$$

$$109 \quad (2.2) \quad \phi(X) = g(X), \quad X \in \Gamma_D,$$

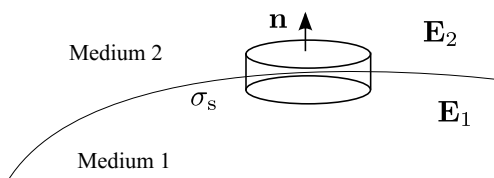
$$110 \quad (2.3) \quad \frac{\partial \phi(X)}{\partial \mathbf{n}_{\Gamma_N}} = p(X), \quad X \in \Gamma_N.$$



99 FIG. 2.1. *Four essential steps in a PIC loop.*



(a) Computation domain including the interface



(b) Electric flux jump across the interface

100 FIG. 2.2. *A sketch of the interface problem and interface condition.*

111 Here,  $\Omega \in \mathbb{R}^3$  is assumed to be an open cuboidal domain, which is divided into two  
 112 subdomains  $\Omega^+$  and  $\Omega^-$  by an interface surface  $\Gamma$  such that  $\overline{\Omega} = \Omega^- \cup \Omega^+ \cup \Gamma$ . The  
 113 boundary  $\partial\Omega$  consists of Dirichlet and Neumann portions, denoted by  $\Gamma_D$  and  $\Gamma_N$ ,  
 114 respectively, such that  $\partial\Omega = \Gamma_D \cup \Gamma_N$  and  $\Gamma_D \cap \Gamma_N = \emptyset$ . The vector  $\mathbf{n}_{\Gamma_N}$  is the unit  
 115 outward normal of  $\Gamma_N$ . See the sketch in Figure 2.2(a). The functions  $\rho$ ,  $g$ , and  $p$   
 116 are the source term, Dirichlet boundary function, and Neumann boundary function,  
 117 respectively. The electric field  $\mathbf{E} = -\nabla\phi(X)$  is discontinuous across the interface  $\Gamma$   
 118 with the following jump conditions imposed:

119 (2.4)  $[\phi(X)]_{\Gamma} = 0,$

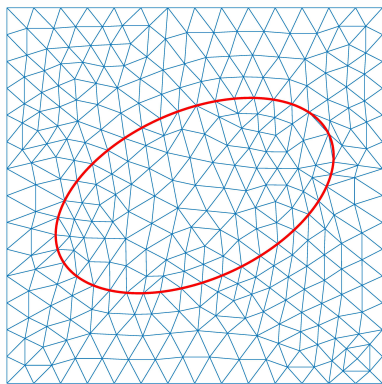
120 (2.5)  $\left[ \varepsilon \frac{\partial\phi(X)}{\partial\mathbf{n}_{\Gamma}} \right]_{\Gamma} = q(X),$

121 where the jump  $[\cdot]_{\Gamma}$  is defined by  $[w(X)]_{\Gamma} := w^+(X)|_{\Gamma} - w^-(X)|_{\Gamma}$ . The vector  $\mathbf{n}_{\Gamma}$   
 122 is the unit normal of  $\Gamma$  pointing from  $\Omega^-$  to  $\Omega^+$ . The material-dependent coefficient  
 123  $\varepsilon(X)$  is discontinuous across the interface. Without loss of generality, we assume it is  
 124 a piecewise constant function defined by

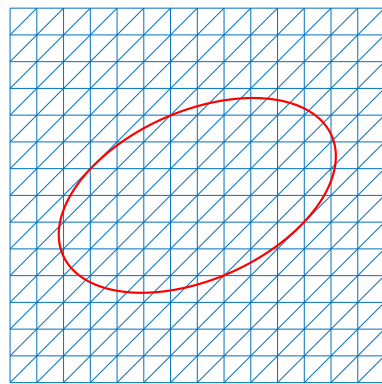
125 
$$\varepsilon(X) = \begin{cases} \varepsilon^-, & X \in \Omega^-, \\ \varepsilon^+, & X \in \Omega^+, \end{cases}$$

126 where  $\min(\varepsilon^+, \varepsilon^-) > 0$ .

127 In many applications of scientific and engineering interest, the shape of the  
 128 interface  $\Gamma$  is usually nontrivial. Traditionally, when solving field problems involving  
 129 complex-shaped objects, an unstructured body-fitting mesh is employed to improve  
 130 accuracy (Figure 2.3(a)). However, a structured mesh, such as Cartesian mesh (Figure  
 131 2.3(b)), is more advantageous in kinetic PIC modeling of plasma dynamics from  
 132 the perspective of computing speed and efficiency, although, it has been limited to  
 133 problems with relatively simple geometries due to accuracy considerations inherited  
 134 from finite-difference-based schemes. To solve this dilemma while taking into account  
 135 both accuracy and efficiency, the IFE-PIC method was developed to handle complex  
 136

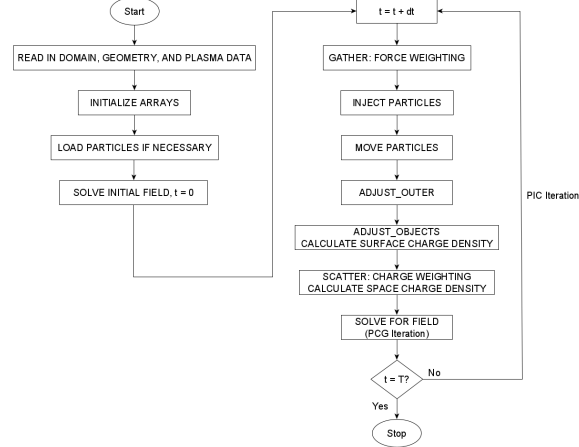


(a) Unstructured body-fitting FE mesh



(b) Structured IFE mesh based on  
Cartesian mesh

127 FIG. 2.3. Illustration of traditional body-fitting FE mesh and *novel* structured IFE mesh.



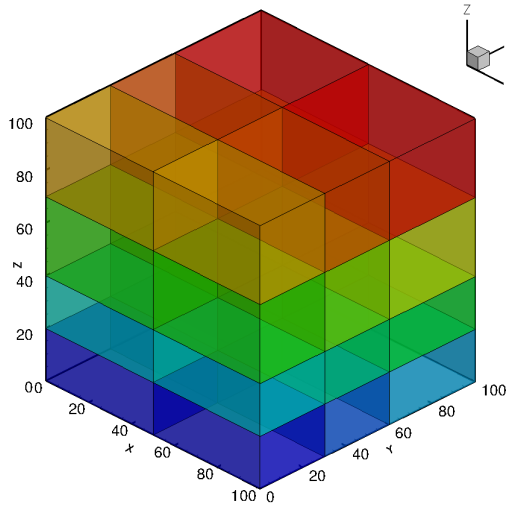
145

FIG. 2.4. Flowchart of serial IFE-PIC.

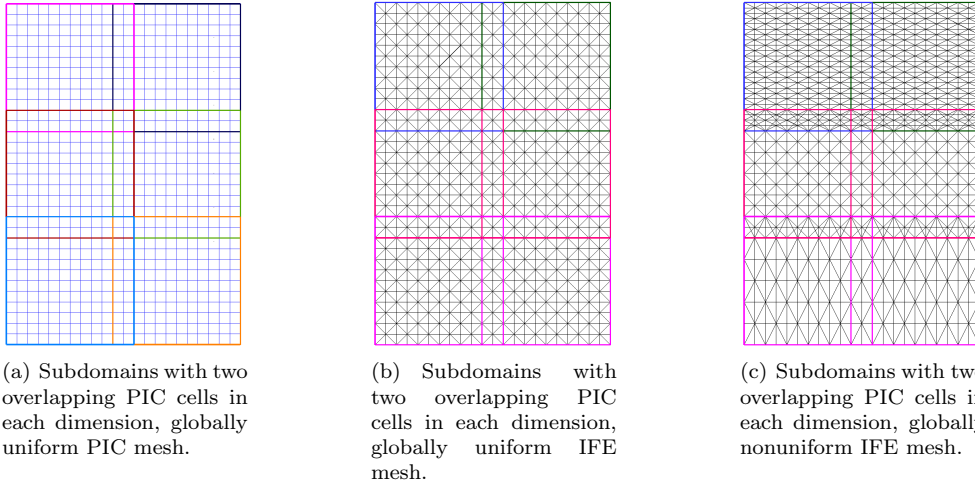
137 interface conditions associated with irregular geometries while maintaining the com-  
 138 putational speed of the Cartesian mesh-based PIC. The detailed IFE formulation and  
 139 IFE-PIC steps are archived in [40], and the flowchart of the serial IFE-PIC algorithm  
 140 is shown in Figure 2.4. Over the past few years, the IFE-PIC method has matured to  
 141 successfully model plasma dynamics problems arising from many space applications,  
 142 such as ion thruster grid optics [13, 53, 55, 56], ion propulsion plume-induced contam-  
 143 ination [57, 80, 77], charging of lunar and asteroidal surfaces [20, 35, 36, 38, 39, 84],  
 144 and dust transport dynamics around small asteroids [85].

149 **2.2. 3-D domain decomposition in PIFE-PIC.** In our PIFE-PIC algorithm,  
 150 the 3-D computational domain is decomposed along each dimension using the message  
 151 passing interface (MPI) architecture (Figure 2.5). The domain is first decomposed  
 152 into cuboid blocks with the same PIC mesh resolution. Each subdomain is handled by  
 153 a processor for both field-solve and particle-push procedures of the PIC method. Two  
 154 overlapping PIC cells (“guard cells”) in each dimension are used in PIFE-PIC (Figure  
 155 2.6) taking advantage of the existing data structure of the serial IFE-PIC which has  
 156 one layer of “guard cells” for global particle boundary conditions. Therefore, the  
 157 boundaries of each subdomain are either on the global boundary or in the interior of  
 158 its neighboring subdomains. Local IFE mesh is then generated for each subdomain.  
 159 By virtue of the IFE formulation, PIC and IFE can use different mesh resolutions.  
 160 In PIFE-PIC, PIC mesh is globally uniform to better balance the loads of particles  
 161 among subdomains (processors). However, IFE mesh could be globally nonuniform  
 162 but still locally uniform within each subdomain. The data interaction between IFE  
 163 and PIC meshes of different resolutions is described in details in [57]. Figures 2.6  
 164 and 2.7 illustrate the 2-D and 3-D views of the domain decomposition and different  
 165 resolutions.

170 **2.3. Parallel algorithm for IFE field solver.** For the parallel electrostatic  
 171 field solver, Dirichlet-Dirichlet domain decomposition with overlapping cells is used  
 172 to distribute the subdomains among multiple MPI processes [8]. For each subdo-  
 173 main, the IFE solver is the same as the sequential IFE method with Dirichlet bound-  
 174 ary conditions [40, 54]. These Dirichlet boundary conditions are imposed at the  
 175 boundaries of the subdomain, which are interior for the neighboring subdomains

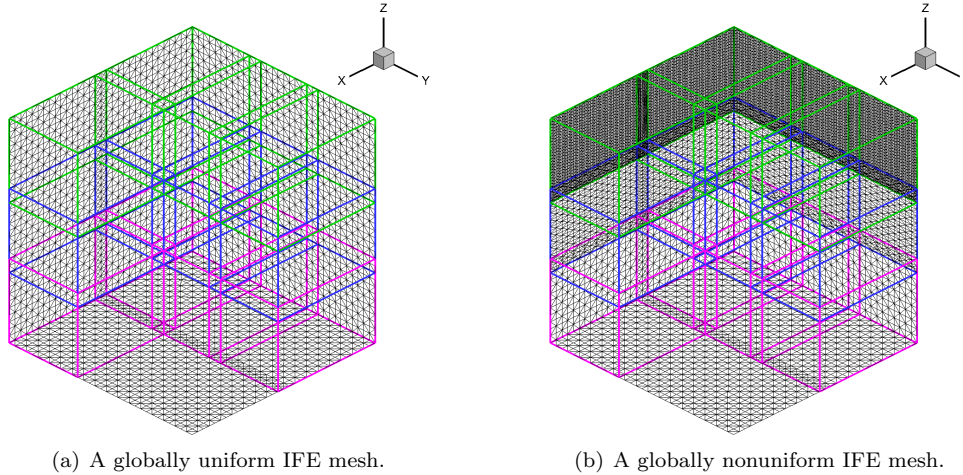


146 FIG. 2.5. 3-D domain decomposition for PIC blocks. Overlapping cells are not displayed. In  
 147 this example, the global domain is decomposed into  $2 \times 3 \times 4$  subdomains. The blue-red color scale  
 148 indicates the MPI rank of each subdomain.



166 FIG. 2.6. 2-D projection showing the domain decomposition for PIC and IFE with overlapping  
 167 cells and different resolutions. The thick colored edges represent boundaries of each subdomain,  
 168 including one layer of guard cells in each dimension. Therefore, there are two overlapping layers of  
 169 PIC cells in each dimension.

176 (Figure 2.8, left). Therefore, the field solutions at respective neighboring subdomains  
 177 are used as Dirichlet boundary conditions for each subdomain. At each field-solve  
 178 step of PIC, domain decomposition method (DDM) iterations among subdomains are  
 179 performed such that the solutions of the overlapping cells are exchanged and updated  
 180 as the new Dirichlet boundary conditions for the respective neighboring subdomains.  
 181 We denote this level of iteration as the DDM iteration. The relative error  $e_{\text{rel}}$  of DDM  
 182 is defined with the  $L^2$  norm as below:



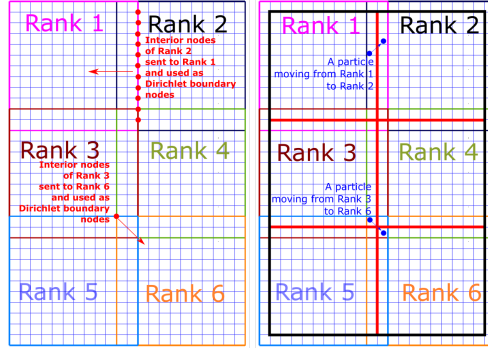
183 FIG. 2.7. 3-D view of globally uniform and nonuniform IFE meshes. The IFE mesh for each  
 184 subdomain is uniform (locally) but could be nonuniform for different subdomains (globally).

185 (2.6) 
$$e_{\text{rel}} = \frac{\|\phi_{\text{new}} - \phi_{\text{old}}\|_{L^2}}{\|\phi_{\text{old}}\|_{L^2}},$$
  
 186

187 where  $\phi_{\text{new}}$  and  $\phi_{\text{old}}$  denote solutions at the new and old steps in the DDM iteration,  
 188 respectively. Within the field-solve part at each PIC step, DDM iterations are carried  
 189 out till the relative error reaches a preset tolerance or reaches the preset maximum  
 190 number of DDM iterations. It is noted here that since PIFE-PIC uses domain decom-  
 191 position in all 3 dimensions, which means there will be surfaces (side by side), edges  
 192 (2-D diagonal), and vertices (3-D diagonal) shared by two neighboring subdomains,  
 193 such MPI data exchange will be carried out at guard cell nodes on “surfaces” (+/−  
 194 neighbor in one direction, such as Rank 1 and Rank 2 in Figure 2.8), “edges” (+/−  
 195 neighbor in two directions, such as Rank 3 and Rank 6 in Figure 2.8), and “vertices”  
 196 (+/− neighbor in three directions).

197 **2.4. Parallel scheme for PIC procedures.** In PIFE-PIC, simulation particles  
 198 belonging to the same subdomain are stored together on the processor that solves the  
 199 electrostatic field of the same subdomain (Figure 2.8, right). In this sense, “particle  
 200 quantities” and “field quantities” of each subdomain are handled by the same proces-  
 201 sor. Each processor (MPI rank) handles its own particles belonging to its domain  
 202 without guard cells (see Figure 2.5). In particle-push, particles crossing the inner  
 203 boundaries are sent to the corresponding rank based on their destination positions.  
 204 Note that such particle motion includes similar cases as data exchange for field-solve,  
 205 which are “crossing one surface” (+/− neighbor in one direction, such as Rank 1  
 206 and Rank 2 in Figure 2.8), “crossing an edge (two surfaces)” (+/− neighbor in two  
 207 directions, such as Rank 3 and Rank 6 in Figure 2.8), and “crossing a vertex (three  
 208 surfaces)” (+/− neighbor in three directions).

234 **2.5. Flowchart for PIFE-PIC.** Figure 2.9 shows the flowchart of PIFE-PIC.  
 235 The steps in red are major steps involving MPI operations associated with domain  
 236 decomposition. In total, there are three levels of iteration in PIFE-PIC. The first  
 237 level is the matrix-solving iteration which uses the preconditioned conjugate gradi-  
 238 ent (PCG) algorithm (PCG level). The second one checks the relative error in the



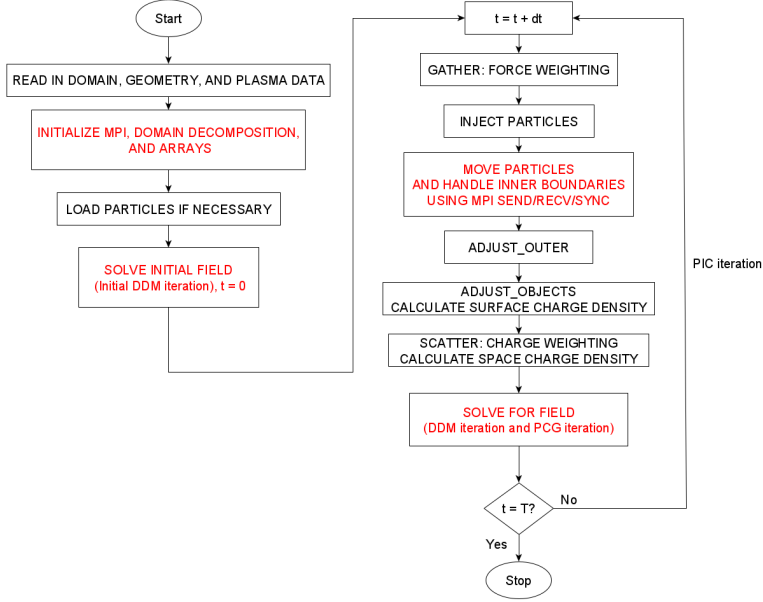
209     FIG. 2.8. MPI data exchange among neighboring subdomains within DDM iteration. In both  
 210 subfigures, the boundaries of the subdomains (with guard cells) of Ranks 1 to 6 are highlighted by  
 211 different colors, which are the same as the colors of the text “Rank” in the corresponding subdomains.  
 212 In the right subfigure, the thick red and black lines, which are the boundaries of the subdomains  
 213 without guard cells, represent the inner and outer particle boundaries, respectively. Left: for field-  
 214 solve operations: on the interior boundaries of the subdomains with guard cells, the nodes at a certain  
 215 subdomain’s boundary (e.g., Rank 1’s boundary nodes) are also interior nodes of its neighboring  
 216 subdomain (e.g., Rank 2). Therefore, the field quantities stored on interior nodes of Rank 2 are sent  
 217 to Rank 1 and used as Dirichlet boundary nodes. Since PIFE-PIC has 3-D domain decomposition,  
 218 such MPI data exchange will be carried out at guard cell nodes on “surfaces” (+/- neighbor in one  
 219 direction, such as Rank 1 and Rank 2), “edges” (+/- neighbor in two directions, such as Rank 3  
 220 and Rank 6), and “vertices” (+/- neighbor in three directions, not shown on this 2-D illustration).  
 221 As for the nodes on the outer boundaries, which are the boundary of the entire problem domain,  
 222 they will be handled based on the given boundary conditions of the entire problem domain, not by the  
 223 MPI data exchange. Right: For particle-push operations: each processor handles its own particles  
 224 belonging to its own subdomain without guard cells (see Figure 2.5). In particle-push, particles  
 225 crossing the inner particle boundaries are sent to the corresponding rank based on their destination  
 226 positions. Such particle motion also includes similar cases as data exchange for field-solve, which  
 227 are “crossing one surface” (+/- neighbor in one direction, such as Rank 1 and Rank 2), “crossing  
 228 an edge (two surfaces)” (+/- neighbor in two directions, such as Rank 3 and Rank 6), and “crossing  
 229 a vertex (three surfaces)” (+/- neighbor in three directions, not shown on this 2-D illustration).  
 230 For charge-weighting on the inner particle boundary, contributions from all neighboring subdomains  
 231 without guard cells should be *all* summed. As for the particles crossing the outer particle boundaries,  
 232 they will be handled based on the given particle boundary conditions of the entire problem domain,  
 233 not by the MPI data exchange.

239 iterations of the domain decomposition method (DDM level). The third one tracks  
 240 the solution of each PIC step (PIC level).

242     **3. Code validation.** We apply the PIFE-PIC code to simulate the charging  
 243 of a small dielectric sphere immersed in a collisionless and stationary plasma in the  
 244 OML sheath regime. Successful validations of the serial IFE-PIC against analytic  
 245 OML solutions are presented in earlier work [40, 38].

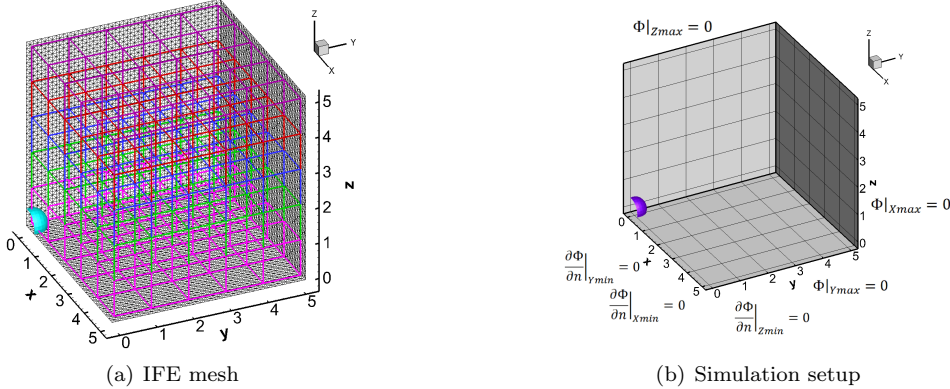
246     **3.1. Problem description and simulation setup.** We consider a stationary,  
 247 collisionless hydrogen plasma of equal ion and electron temperatures ( $T_i = T_e$ ). The  
 248 analytic expressions for ion and electron densities in the plasma are given by the  
 249 revised OML theory [76, 19]. Therefore, the analytic potential profile near the sphere  
 250 can be numerically solved from Poisson’s equation in spherical coordinates.

251     **3.1.1. Computation domain and mesh.** In the simulation, we use a compu-  
 252 tation domain of a  $5 \times 5 \times 5$  Debye cube with a globally uniform PIC mesh with the



241

FIG. 2.9. Flowchart of PIFE-PIC.



262     FIG. 3.1. IFE mesh and setup used in the 3-D OML sheath problem for code validation. In  
263     this example, the global domain is decomposed into  $5 \times 5 \times 5$  subdomains. Different layers (along z-  
264     direction) of the subdomains are highlighted in different colors. 1/8 of the sphere is centered at the  
265     origin.

253     size of  $h = 0.1\lambda_D$  in all dimensions, where  $\lambda_D$  is the Debye length of the plasma. The  
254     entire simulation domain has  $50 \times 50 \times 50 = 125,000$  PIC cells which is  $125,000 \times 5 =$   
255     625,000 tetrahedral FE/IFE cells as each cuboid PIC cell is partitioned into 5 tetrahe-  
256     dral FE/IFE cells in 3-D IFE-PIC [40, 38]. The IFE mesh size is also globally uniform  
257     and the same as that of the PIC mesh. The dielectric sphere is centered at  $(0, 0, 0)$   
258     with a radius of  $R_s = 0.401$ . Due to symmetry in all three dimensions, only 1/8 of  
259     the sphere is included in the domain. The entire domain is partitioned into  $5 \times 5 \times 5$   
260     subdomains with each subdomain computed by one MPI process. Figure 3.1 shows  
261     the 3-D IFE mesh and setup used in the simulation.

266       **3.1.2. Field setup.** At  $X_{\max}$ ,  $Y_{\max}$ , and  $Z_{\max}$  boundaries, the potentials are set  
 267 to 0 as the reference potential. At  $X_{\min}$ ,  $Y_{\min}$ , and  $Z_{\min}$  boundaries, zero-Neumann  
 268 boundary conditions are applied due to symmetry (Figure 3.1(b)). The relative per-  
 269 mittivity of the sphere is set to 4. The floating potential of the sphere is calculated  
 270 from the nonhomogeneous flux jump condition at the sphere surface.

271       **3.1.3. Particle setup.** The simulation is carried out using the realistic ion-to-  
 272 electron mass ratio of  $m_i/m_e = 1,836$ . Particles are preloaded into the domain before  
 273 the initial field solution and injected into the domain at  $X_{\max}$ ,  $Y_{\max}$ , and  $Z_{\max}$  within  
 274 each PIC step. Particles hitting the  $X_{\min}$ ,  $Y_{\min}$ , and  $Z_{\min}$  boundaries are reflected due  
 275 to symmetry. Particles hitting the  $X_{\max}$ ,  $Y_{\max}$ , and  $Z_{\max}$  are absorbed and removed  
 276 from the simulation. The normalized time step size was set to be 0.01. There were  
 277 125 particles ( $5 \times 5 \times 5$ ) per species per cell being loaded/injected into the domain.

278       **3.2. Simulation results.** The simulation of the validation case finished in about  
 279 2 hours for a total of 50,000 PIC steps on the *Foundry* cluster provided by the Center  
 280 of High-Performance Computing Research at Missouri University of Science and  
 281 Technology. The computing nodes are configured with Dell C6525 nodes each having  
 282 four node chassis with each node containing dual 32-core AMD EPYC Rome 7452  
 283 CPUs with 256 GB DDR4 RAM and six 480 GB SSD drives in RAID 0. All other  
 284 simulations presented in this work were also carried out on the same cluster.

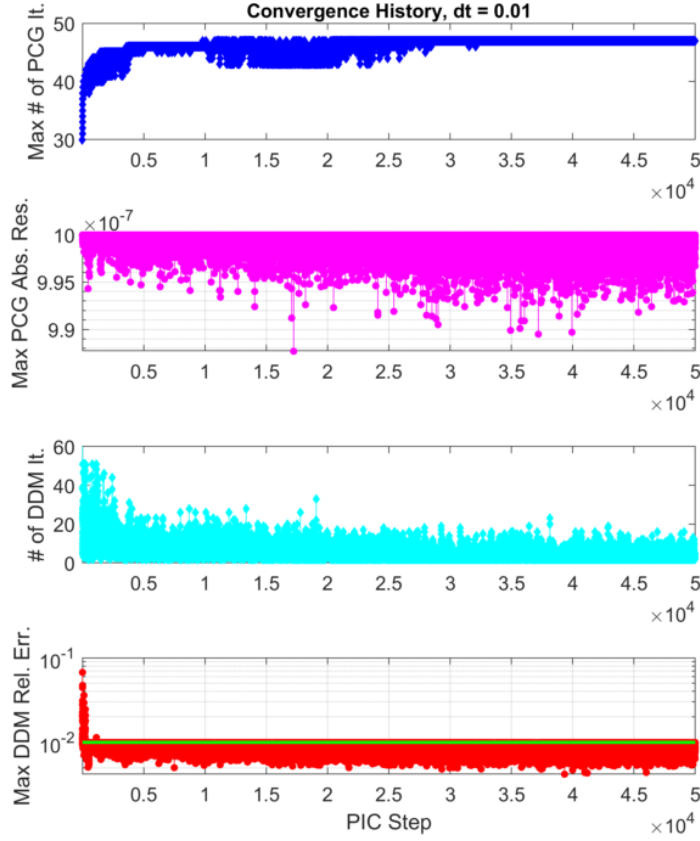
285       For this test case, the maximum number of PCG iterations was set to 50 with  
 286 a tolerance of  $1 \times 10^{-6}$  for absolute residual, while the maximum number of initial  
 287 DDM iterations (solving the initial electrostatic field before main PIC loop starts)  
 288 was set to 150 and the maximum number of DDM iterations at each PIC iteration  
 289 step was set to 50 with a tolerance of  $1 \times 10^{-2}$ . The simulation was set to run 50,000  
 290 PIC steps.

291       **3.2.1. Initial field solution.** The initial field solution (the zeroth PIC step)  
 292 took about 100 DDM iterations which are more than what is needed at each step  
 293 of the main PIC loop, to converge in terms of the relative error  $1 \times 10^{-2}$ . The idea  
 294 of setting a relatively larger DDM iteration number is to obtain a better initial field  
 295 for the main PIC loop. Since the initial field was solved only once, the extra DDM  
 296 iterations contributed little to the overall wall-clock time of the entire simulation.

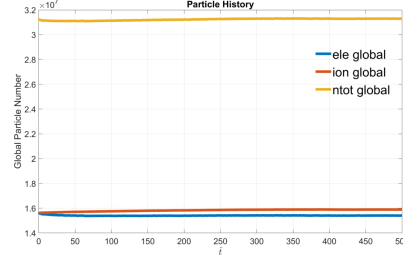
297       **3.2.2. Solution history of main PIC loop.** Figure 3.2 shows the field solution  
 298 convergence history including the maximum absolute PCG residual and maximum  
 299 DDM relative error as a function of PIC steps in the main PIC loop. A few phenomena  
 300 are observed here:

- 301       1. For most PIC steps, PCG took about 45–50 iterations to reach the tolerance  
 302 of  $1 \times 10^{-6}$ . The “max” in the vertical axis stands for “maximum among all  
 303 subdomains” (first plot);
- 304       2. The maximum PCG absolute residual of the matrix solver has been main-  
 305 tained below  $1 \times 10^{-6}$  (second plot);
- 306       3. At early PIC steps, most DDM steps took about tens of iterations to converge  
 307 below  $1 \times 10^{-2}$ , while later on as PIC approaches steady state, most DDM  
 308 steps were able to converge in less than 15 iterations (third and forth plots).

311       Figure 3.3 shows the global particle number history. At the steady state, there  
 312 are approximately  $3.12 \times 10^7$  particles in the entire global domain. It is also shown  
 313 that the numbers of particles reached steady state at normalized simulation time of  
 314 about  $\hat{t} = 100$ .



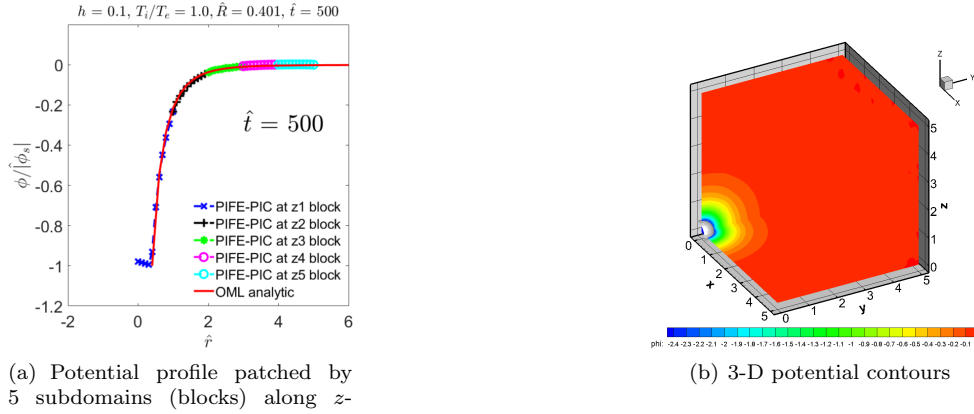
309 FIG. 3.2. Field convergence history of the code validation test case, PCG absolute residual, and  
 310 DDM relative error. The green line on maximum DDM relative error plot is the DDM tolerance.



315 FIG. 3.3. Global particle history of the code validation test case. “*ntot*” is the total number of  
 316 particles (electrons plus ions).

317 **3.2.3. Comparison with analytic solution.** Figure 3.4 shows the comparison  
 318 between PIFE-PIC simulation results against analytic solution for the OML sheath  
 319 problem as well as a 3-D potential contour. The potential profile agrees very well with  
 320 the analytic solution, as also shown in earlier work with the serial IFE-PIC [38, 40].

323 **3.3. Performance profiling.** Table 3.1 shows the detailed timer profile of PIFE-  
 324 PIC on the validation case for the entire 50,000 PIC steps, in terms of the per-  
 325 centage of total wall-clock time of key procedures in PIFE-PIC, namely, “gather,”



(a) Potential profile patched by 5 subdomains (blocks) along  $z$ -direction

(b) 3-D potential contours

321 FIG. 3.4. Validation of OML sheath solution: PIFE-PIC versus analytic and 3-D potential  
322 contours.

342 TABLE 3.1  
343 Time percentage breakdown for all 50,000 PIC steps.

Computing step	Percent of total wall-clock time		
	In rank0001	In rank0050	In rank0100
Total wall-clock time	100.00%	100.00%	100.00%
Initialization time	0.05%	0.05%	0.05%
Main PIC Loop time	99.95%	99.95%	99.95%
Total gather time	11.21%	11.01%	10.49%
Total particle-push time	47.10%	47.10%	47.10%
Total particle-push-comm (AdjustOuter local) time*	24.89%*	24.88%*	24.89%*
Total adjust-objects time	3.45%	3.45%	3.45%
Total scatter time	3.83%	3.83%	4.10%
Total field-solve time	31.79%	31.78%	31.78%
Total field-solve-phibc (Update Phi BC) time**	4.54%**	22.82%**	22.93%**
Total other time	2.62%	2.83%	3.08%

\*Included in the “particle-push time”

\*\*Included in the “field-solve time”

326 “particle-push,” “particle-push-comm” (particle adjustment at local boundaries and  
327 communication among subdomains), “adjust-objects” (particle collection and charge  
328 deposition), “scatter,” “field-solve,” “field-solve-phibc” (communication among sub-  
329 domains and update of local potential boundary conditions), and “other” (including  
330 particle injection at global boundaries and calculation of electric field), for selected  
331 CPUs/subdomains (also the MPI ranks). Three subdomains (MPI ranks) are chosen,  
332 namely, rank0001, rank0050, and rank0100.

333 Particularly, for “field-solve,” the communication time (“field-solve-phibc”) is sig-  
334 nificantly higher for rank0050 and rank0100, indicating they spent more time in the  
335 “MPI-wait” part of the communication (because all subdomains did MPI-send/receive  
336 with similar load). This means that they were faster than rank0001 in the part  
337 of “field-solve.” This is because, as shown in Figure 3.1(a), rank0001 is the only  
338 subdomain with interface, which adds extra work to rank0001 compared with other  
339 interface-free subdomains. Therefore, in order to improve the parallel efficiency, the  
340 working load of rank0001 should be reduced. This strategy will be utilized in the next  
341 section.

344 The computing time of “particle-push” essentially depends on the number of  
345 simulation particles in the domain, which also affects the accuracy and smoothness  
346 of the source term for Poisson’s equation. Therefore, in practical PIC simulations,

347 large numbers of particles are preferred when computing resources are available. The  
 348 computing time of “field-solve” (including communication) depends on at least two  
 349 major factors: 1) the size of each subdomain (number of mesh cells and nodes) and  
 350 balance among subdomains, and 2) the number of DDM iterations. The size of each  
 351 subdomain can be determined by the domain decomposition configurations, while the  
 352 number of DDM iterations is affected by the DDM relative error tolerance and the  
 353 maximum number of DDM iterations. In the following section, we investigate the  
 354 strong scaling performance of PIFE-PIC by varying 1) the size of each subdomain  
 355 and 2) the maximum number of DDM iterations.

356 **4. Parallel efficiency: Strong scaling.** For most large-scale problems of practical  
 357 interests, the problem size is usually determined by the physical phenomena to be resolved. Therefore, to test the parallel efficiency of PIFE-PIC, we use the *strong*  
 358 scaling approach such that the problem size is *fixed* while the number of processors  
 359 increases. For this set of tests, the problem size was fixed as a  $10 \times 10 \times 10$  Debye cube  
 360 with a globally uniform PIC mesh size of  $h = 0.1\lambda_D$  in all dimensions. The entire  
 361 simulation domain has  $100 \times 100 \times 100 = 1$  million PIC cells (5 million tetrahedral  
 362 FE/IFE cells) and about 54 million particles. For these runs, the maximum number  
 363 of PCG iteration was set to 1,000 with a tolerance of  $1 \times 10^{-6}$  for absolute residual.  
 364 For the initial field solution, the maximum number of DDM iteration was set to 100,  
 365 while for each step within the main PIC loop, the maximum number of DDM iteration  
 366 was set to be 10 or 6 for two different groups with same tolerance of  $1 \times 10^{-2}$ . The  
 367 normalized time step size was set to be 0.01 and all simulations ran for 20,000 PIC  
 368 steps. The speedup is defined as  $S = T_s/T_p$ , where  $T_s$  is the serial runtime and  $T_p$  is  
 369 the parallel runtime on  $p$  MPI processes. The strong scaling parallel efficiency is then  
 370 defined as  $E = S/p = T_s/(p \cdot T_p)$ . We chose two groups of configurations to test the  
 371 parallel efficiency:  
 372

- Group I: Using at most 10 DDM iterations per main-loop PIC step;
- Group II: Using at most 6 DDM iterations per main-loop PIC step.

373 Table 4.1 lists the domain decomposition configurations for each test case, along  
 374 with the sizes of smallest and biggest subdomains in terms of number of cells in each  
 375 direction. The different sizes of subdomains indicate load imbalances among CPUs,  
 376 which may affect the MPI communication cost as shown in Table 3.1, and thus affect  
 377 the parallel efficiency. Based on the above discussion for Table 3.1, Rank 1, which  
 378 handles the interface part, has extra computational cost compared with other CPUs,  
 379 hence should handle smaller subdomain in order to better balance the working loads.  
 380 Therefore, we utilize the following strategy to decompose the computation domain  
 381 in each direction: make the first subdomain (block) smaller (but still enclosing the  
 382 object) and the rest *of the same size*. For instance, to decompose the 100 cells in one  
 383 direction into 6 blocks, we use the configuration of  $(1 \times 10 + 5 \times 18 = 100)$ , i.e., the first  
 384 block takes 10 cells, and the rest 5 blocks take 18 cells each, totally 100 cells in one  
 385 direction. For other numbers of blocks to distribute the 100 cells in each direction,  
 386 we use the following configurations:  
 387

- 4 blocks:  $1 \times 19 + 3 \times 27 = 100$ ;
- 5 blocks:  $1 \times 12 + 4 \times 22 = 100$ ;
- 6 blocks:  $1 \times 10 + 5 \times 18 = 100$ ;
- 7 blocks:  $1 \times 10 + 6 \times 15 = 100$ .

388 Table 4.2 lists the total wall-clock time, speedup, and parallel efficiency of each  
 389 case for both Group I and Group II. The timer data was taken over all 20,000 PIC  
 390 steps. A few trends are observed here:

393 TABLE 4.1  
 394 *Domain Decomposition Configurations for Strong Scaling Test Cases.*

# of subdomains	DD configurations	Size of smallest subdomain (cells)	Size of biggest subdomain (cells)
1 (serial)	$1 \times 1 \times 1$	$100 \times 100 \times 100$	$100 \times 100 \times 100$
64	$4 \times 4 \times 4$	$19 \times 19 \times 19$	$27 \times 27 \times 27$
80	$4 \times 4 \times 5$	$19 \times 19 \times 12$	$27 \times 27 \times 22$
100	$4 \times 5 \times 5$	$19 \times 12 \times 12$	$27 \times 22 \times 22$
125	$5 \times 5 \times 5$	$12 \times 12 \times 12$	$22 \times 22 \times 22$
150	$5 \times 5 \times 6$	$12 \times 12 \times 10$	$22 \times 22 \times 18$
180	$5 \times 6 \times 6$	$12 \times 10 \times 10$	$22 \times 18 \times 18$
216	$6 \times 6 \times 6$	$10 \times 10 \times 10$	$18 \times 18 \times 18$
252	$6 \times 6 \times 7$	$10 \times 10 \times 10$	$18 \times 18 \times 15$
294	$6 \times 7 \times 7$	$10 \times 10 \times 10$	$18 \times 15 \times 15$
343	$7 \times 7 \times 7$	$10 \times 10 \times 10$	$15 \times 15 \times 15$

417 TABLE 4.2  
 418 *Strong Scaling Test Results.*

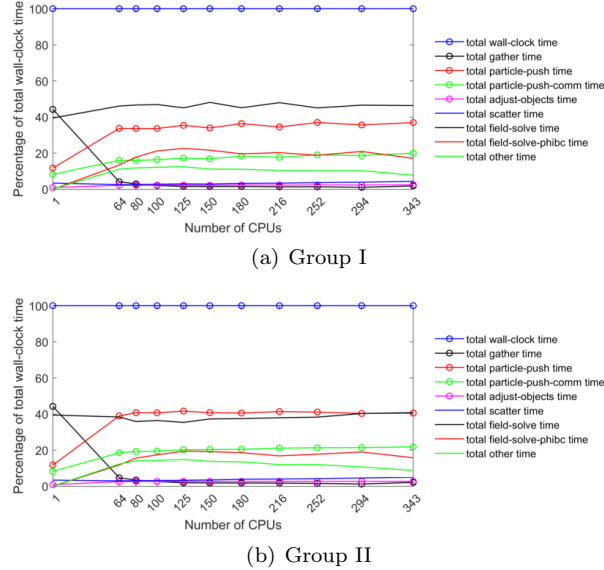
# of sub-domains	Total time $T_I$ (min)	Speedup $S_I$	Efficiency $E_I$	Total time $T_{II}$ (min)	Speedup $S_{II}$	Efficiency $E_{II}$
1 (serial)	12,084	1	100.00%	12,084	1	100.00%
64	200	60.47	94.49%	173	69.77	109.02%
80	163	73.92	92.40%	135	89.59	111.99%
100	143	84.25	84.25%	113	106.57	106.57%
125	111	108.75	87.00%	96	125.98	100.79%
150	99	122.10	81.40%	85	142.49	94.99%
180	80	151.41	84.11%	74	164.01	91.12%
216	74	163.90	75.88%	62	193.57	89.62%
252	63	191.55	76.01%	58	209.40	83.10%
294	65	186.26	63.35%	60	200.95	68.35%
343	57	212.76	62.03%	53	227.99	66.47%

398 1. In general, the parallel efficiency of cases in Group II (at most 6 DDM iterations per PIC step) is higher than the corresponding case in Group I (at most 400 10 DDM iterations per PIC step). This is obviously because fewer DDM 401 iterations per PIC step would save more time in the field-solve part, thus 402 resulting in a shorter total wall-clock time.

403 2. For both Group I and Group II, the parallel efficiency starts quite high (close 404 to or even above 100%) and gradually decays when the CPU number and 405 communications increase.

406 3. As mentioned above, we also notice that for Group II, some parallel cases 407 achieved  $>100\%$  *superlinear speedup* in this strong scaling. One possible 408 reason is that, with domain decomposition, the number of mesh nodes of 409 each subdomain is significantly less than that of the entire domain (which 410 is the serial case). Therefore, the matrix size of each subdomain is much 411 smaller than that of the serial case. Since the PCG solver scales at  $N \log(N)$  412 where  $N$  is the size of the matrix, the PCG solution of parallel cases are 413 much faster than that of the serial case. Therefore, when the communication 414 overhead is not significant, superlinear speedup may occur. As the number of 415 CPUs increases, the superlinear speedup is suppressed by the communication 416 overhead.

419 Figure 4.1 plots the percentage of total wall-clock time to show the performance 420 of PIFE-PIC for each domain decomposition configuration in Group I and Group II.



431        FIG. 4.1. *Percentage of total wall-clock time of key procedures, for each domain decomposition*  
 432 *configuration.*

421 Some trends are also observed: 1) The percentage breakdown of the key PIC pro-  
 422 cedures is fairly consistent across all parallel configurations. 2) The “field-solve” step  
 423 took about 40% of the total wall-clock time across all parallel cases, whereas about  
 424 20% (of the total wall-clock time) was spent on the “field-solve-phibc” step. Based  
 425 on more detailed data, which is omitted due to the page limitation, we also observe  
 426 that the percentage of the time for “field-solve-phibc” varies within about 10% for all  
 427 subdomains/ranks. This is much better balanced than that shown in Table 3.1. 3)  
 428 The “particle-push” step takes about 35–40% of the total wall-clock time consistently  
 429 across all parallel cases, whereas about 20% (of the total wall-clock time) is spent on  
 430 the “particle-push-comm” step.

433        **5. Application to lunar crater charging.** In this section, we apply PIFE-  
 434 PIC to simulate the plasma charging at a lunar crater under average solar wind  
 435 (SW) conditions to demonstrate the large-scale simulation capability of PIFE-PIC.  
 436 In the following, we will first briefly describe the lunar surface charging problem, then  
 437 introduce the setup of the simulation, and finally present the results and discussion.

438        **5.1. Problem description.** The problem considered is SW plasma charging  
 439 near the lunar surface, specifically, near the lunar craters at the terminator region for  
 440 lunar exploration missions. The Moon is directly exposed to the solar radiation and  
 441 various space plasma environments which directly interact with the lunar surface. A  
 442 direct consequence of such interactions is surface charging. Observations have found  
 443 that the potential of the sunlit surface is typically a few tens of volts positive with  
 444 respect to ambient due to photoelectron emission, while that of the surface in shadow  
 445 can be hundreds to thousands of volts negative because of the hot electron flux from  
 446 ambient plasma that can dominate the charging process [10, 23, 32, 33, 34, 73, 75, 83].  
 447 Both solar illumination and plasma flow can have a substantial influence on lunar  
 448 surface charging. At the lunar terminator, the rugged surface terrain, such as that  
 449 near a crater, generates localized plasma wakes and shadow regions which can lead to

466  
467 TABLE 5.1  
Average SW and photoelectron (at 90° Sun elevation angle) parameters.

	Number density $n$ , $\text{cm}^{-3}$	Drifting velocity $v_d$ , $\text{km/s}$	Thermal velocity $v_t$ , $\text{km/s}$	Temperature $T$ , $\text{eV}$	Debye length $\lambda_D$ , $\text{m}$
SW electron	8.7	468	1453	12	8.73
SW ion	8.7	468	31	10	N/A*
Photoelectron	64	N/A*	622	2.2	1.38

\*N/A denotes “not applicable”

450 strong differential charging at the surface [9, 71, 82]. Both the localized plasma flow  
451 field and the charged lunar surface are expected to have substantial influence on the  
452 charging of spacecraft/landers/rovers/habitats for future surface missions.

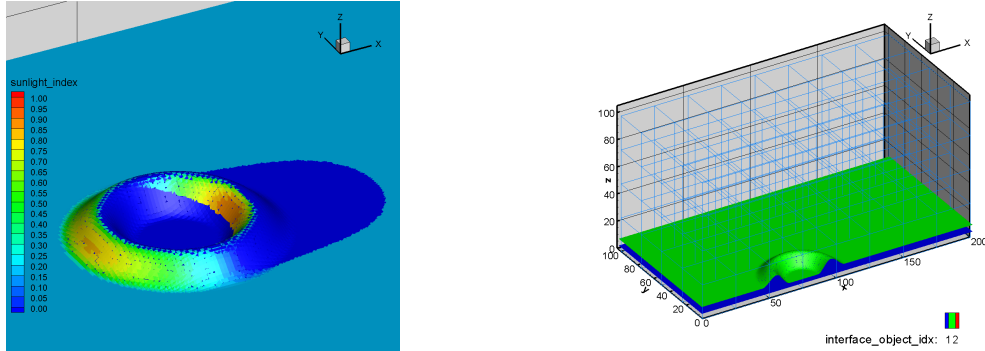
453 The lunar surface is covered by the lunar regolith layer which separates the solid  
454 bedrock from the plasma environment. The regolith layer in most areas is about  
455 4 to 20 meters thick [69, 74]. A complete model of plasma charging on the lunar  
456 surface needs to explicitly take into account the properties of the regolith layer, such  
457 as permittivity, layer thickness, and the lunar electrical ground.

458 The serial version of IFE-PIC method has been successfully applied to simulations  
459 of lunar plasma charging [39]. In order to illustrate the high performance computing  
460 capability of the PIFE-PIC package in this paper, we apply PIFE-PIC to a much larger  
461 scale parallel simulation with a larger simulation domain including a lunar crater and  
462 much more simulation particles. The plasma environment is chosen to be the average  
463 SW and photoelectron parameters at the lunar surface [82], as shown in Table 5.1. It  
464 is noted here that the Debye length of photoelectrons at 90° Sun elevation angle (1.38  
465 m) is used as the reference length to normalize spatial dimensions in PIFE-PIC.

## 468 5.2. Simulation setup.

469 **5.2.1. Lunar crater geometry and simulation domain.** In PIFE-PIC, the  
470 geometry of the lunar crater is realized through an algebraic equation describing the  
471 surface terrain in the form of  $z = z(x, y)$  where  $z$  denotes the surface height. For the  
472 lunar crater considered here, the shape is realized by a few characteristic parameters  
473 such as inner-rim radius, outer-rim radius, depth, rim height, etc. (Figure 5.1(a))  
474 according to the *Lunar Sourcebook* [50]. The specific diameter of a real lunar crater  
475 can be measured through NASA Jet Propulsion Laboratory’s website, Moon Trek  
476 [70]. The crater considered in this study has these characteristic dimensions: inner-  
477 rim radius  $10.5 \times 1.38 = 14.49$  m, top-rim radius  $20.2 \times 1.38 = 27.88$  m, outer-rim radius  
478  $30.9 \times 1.38 = 42.64$  m, and top height  $6.7 \times 1.38 = 9.25$  m. Details of the approach to  
479 set up the lunar crater geometry is given in [68].

480 The simulation domain has  $200 \times 100 \times 100 = 2$  million PIC cells (10 million tetra-  
481 hedral FE/IFE cells) including half of the lunar crater due to symmetry with respect  
482 to the  $X$ - $Z$  plane at  $y = 0$  (Figure 5.1(a)). Each PIC cell is a  $1.38 \times 1.38 \times 1.38$  cube.  
483 In physical units, the domain size is approximately 276 m by 138 m by 138 m. At  
484 the  $Z_{\min}$  boundary, the simulation domain includes a layer of the lunar bedrock with  
485 a thickness of  $L_{\text{bedrock}} = 4.5 \times 1.38 = 6.21$  m. On top of the bedrock is a layer of di-  
486 electric regolith with a thickness of  $L_{\text{regolith}} = (9.5 - 4.5) \times 1.38 = 6.9$  m. The relative  
487 permittivities of the lunar regolith layer and the bedrock are taken to be  $\epsilon_{\text{regolith}} = 4$   
488 and  $\epsilon_{\text{bedrock}} = 10$ , respectively [50]. Three-dimensional domain decomposition of  
489  $8 \times 4 \times 4$  (total 128 MPI processes) is used to run the simulation (Figure 5.1(b)).



(a) The geometry of the lunar crater realized in PIFE-PIC. Color contours show the “sunlight index” indicating the inner product of Sun vector ( $10^\circ$  above the ground in the  $X - Z$  plane) and local surface normal vector.

(b) The simulation domain including the lunar bedrock (below the blue layer) and the lunar regolith (between the blue and green layers). The light-blue edges show the domain decomposition ( $8 \times 4 \times 4 = 128$  MPI processes).

480

FIG. 5.1. *The lunar crater geometry and simulation domain.*

491

**5.2.2. Particle and field boundary conditions.** Particles representing SW ions and electrons are preloaded and injected into the domain with an angle of  $10^\circ$  towards the surface in the  $X - Z$  plane (Figure 5.1(a)). Particles representing photoelectrons are generated at the sunlit regions according to the local sunlight index. At the global  $X_{\min}$ ,  $X_{\max}$ ,  $Y_{\max}$ , and  $Z_{\max}$  domain boundaries, ambient SW particles are injected. Particles hitting the global  $Y_{\min}$  boundary are reflected due to symmetry. Particles hitting the lunar surface are collected, and their charges are accumulated to calculate surface charging.

492

493

494

495

496

497

498

499

500

501

502

503

504

505

Dirichlet boundary condition of  $\Phi = 0$  is applied at the  $Z_{\max}$  boundary (the unperturbed SW), whereas Neumann boundary condition of zero electric field is applied on all other five domain boundaries. The PCG maximum iterations was set to 150 with a tolerance of  $1 \times 10^{-6}$  for absolute residual. The maximum number of DDM iteration for initial field solution was set to 800, and the maximum number of DDM iteration for each step within the main PIC loop was set to 200 with a tolerance of  $1 \times 10^{-3}$ . The simulation ran for 20,000 PIC steps.

506

**5.3. Convergence history.** The run took about 154 hours to finish 20,000 PIC steps with the time step size of 0.05 (total simulation time till  $\hat{t} = 1,000$ ). Figure 5.2 shows the convergence history of the lunar crater charging simulation including the maximum absolute PCG residual and maximum DDM relative error and particle number histories. It is shown that the field solution residuals and relative errors started to level off near PIC step of 10,000 ( $\hat{t} = 500$ ), and at steady state, the entire domain had about 1.03 billion particles. After  $\hat{t} = 500$ , the autosaved simulation results are all similar. The results presented below are those at  $\hat{t} = 1,000$ .

507

508

509

510

511

512

513

514

515

516

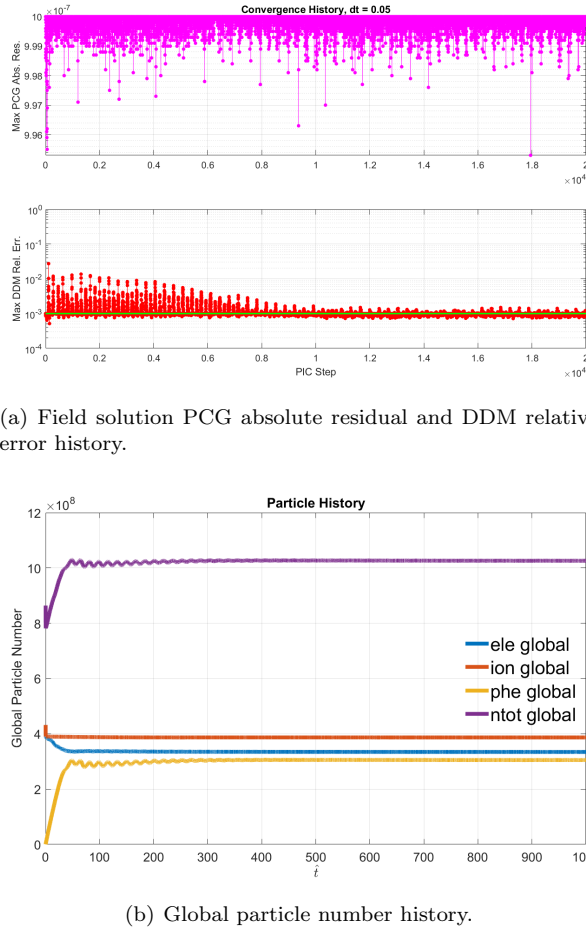
517

518

519

520

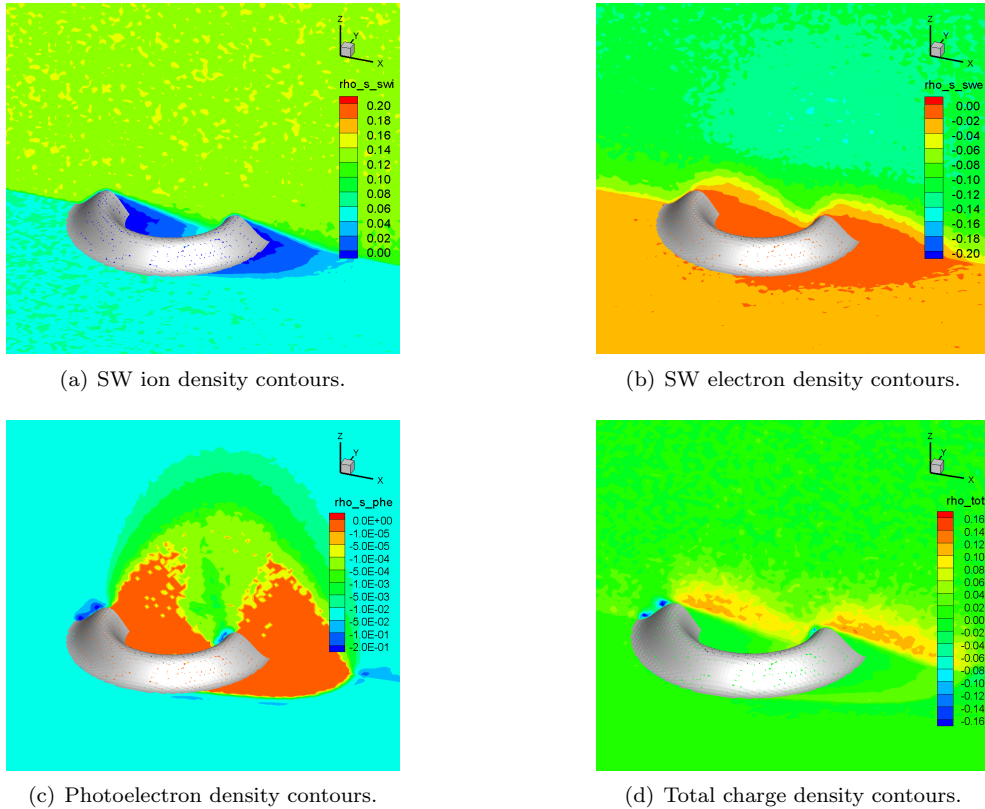
**5.4. Surface charging results.** Figure 5.3 illustrate the density contours of SW ions, solar wind electrons, photoelectrons, and total space charge near the crater. The SW ion and electron density contours clearly exhibit a localized plasma wake formed by the crater rim. The photoelectron density contours clearly exhibit the lack of photoemission in the shadow region. The total space charge density contours show the nonneutral regions associated with the wake caused by the crater rim.

FIG. 5.2. *The lunar crater simulation convergence history.*

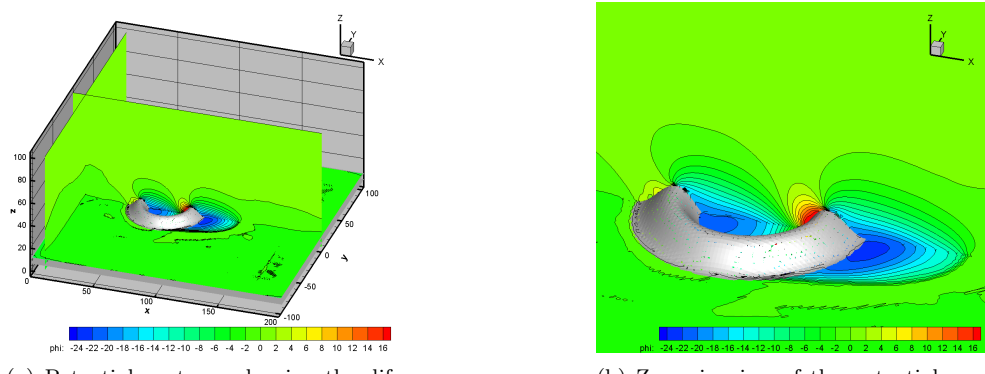
514

524 Figure 5.4 illustrates the potential contours of the domain and near the crater. It  
 525 is shown, for the average SW conditions considered here, the surface potential in the  
 526 sunlit region of the crater is charged to about  $16 \times 2.2 \simeq 35$  V while the surface in the  
 527 shadow region is charged to about  $-24 \times 2.2 \simeq -53$  V. It is noted as this length scale  
 528 is on the order of tens of meters, such differential surface charging will affect the lunar  
 529 surface activities for exploration missions, such as the risk of discharging/arcing and  
 530 horizontal/vertical transport of lofted charged lunar dusts.

533 **6. Summary and conclusion.** In this paper, we presented a most recently  
 534 developed 3-D PIFE-PIC method, for kinetic particle simulations of PMIs especially  
 535 electrostatic surface charging. PIFE-PIC is based on the serial nonhomogeneous elec-  
 536 trostatic IFE-PIC algorithm, which was designed to handle complex interface condi-  
 537 tions associated with irregular geometries while maintaining the computational speed  
 538 of Cartesian mesh-based PIC. Three-dimensional domain decomposition is used in  
 539 both field-solve and particle-push procedures of PIC to distribute the computation  
 540 among multiple processors. A validation case of 3-D OML sheath of a dielectric  
 541 sphere immersed in a stationary plasma was carried out and results agreed well with



521        FIG. 5.3. *Normalized density contours. For electrons, numerical values include a negative*  
 522 *sign indicating the negative charges. The densities are normalized by  $64 \text{ cm}^{-3}$ , and the spatial*  
 523 *dimensions are normalized by 1.38 m.*



531        FIG. 5.4. *Potential contours of lunar crater charging. The potential values are normalized by*  
 532 *2.2 V, and the spatial dimensions are normalized by 1.38 m.*

542 the analytic solution. A series of strong scaling tests were performed to profile the  
 543 parallel efficiency for a problem of fixed size which has 1 million PIC cells (5 million  
 544 tetrahedral FE/IFE cells), about 54 million particles, and running 20,000 PIC steps  
 545 on the Foundry cluster at Missouri University of Science and Technology. Parallel  
 546 efficiency up to approximately 110% superlinear speedup was achieved.

547 An application of PIFE-PIC to a larger problem, SW plasma charging at a lunar  
 548 crater, is presented to show the capability of PIFE-PIC for practical problems of  
 549 science and engineering interest. The lunar crater charging simulation has 2 million  
 550 PIC cells (10 million tetrahedral FE/IFE cells), about 1 billion particles, and running  
 551 for 20,000 PIC steps. The simulation finished in about 154 wall-clock hours with  
 552 domain decomposition of  $8 \times 4 \times 4 = 128$  MPI processes. This demonstrates that PIFE-  
 553 PIC can be utilized to carry out realistic large-scale particle simulations of PMIs  
 554 routinely on supercomputers with distributed memory.

555

## REFERENCES

- 556 [1] S. ADJERID, N. CHAABANE, T. LIN, AND P. YUE, *An immersed discontinuous finite element*  
 557 *method for the Stokes problem with a moving interface*, J. Comput. Appl. Math., 362  
 558 (2019), pp. 540–559.
- 559 [2] S. ADJERID AND T. LIN, *p-th degree immersed finite element for boundary value problems with*  
 560 *discontinuous coefficients*, Appl. Numer. Math., 59 (2009), pp. 1303–1321.
- 561 [3] S. ADJERID, T. LIN, AND Q. ZHUANG, *Error estimates for an immersed finite element method*  
 562 *for second order hyperbolic equations in inhomogeneous media*, J. Sci. Comput., 84 (2020),  
 563 p. 35.
- 564 [4] S. ADJERID AND K. MOON, *An immersed discontinuous Galerkin method for acoustic wave*  
 565 *propagation in inhomogeneous media*, SIAM J. Sci. Comput., 41 (2019), pp. A139–A162.
- 566 [5] J. BAI, Y. CAO, Y. CHU, AND X. ZHANG, *An improved immersed finite element particle-in-cell*  
 567 *method for plasma simulation*, Comput. Math. Appl., 75 (2018), pp. 1887–1899.
- 568 [6] J. BAI, Y. CAO, X.-M. HE, AND P. E, *An implicit particle-in-cell model based on anisotropic*  
 569 *immersed-finite-element method*, Comput. Phys. Commun., 261 (2021), 107655.
- 570 [7] J. BAI, Y. CAO, X.-M. HE, H. LIU, AND X. YANG, *Modeling and an immersed finite element*  
 571 *method for an interface wave equation*, Comput. Math. Appl., 76 (2018), p. 1625–1638.
- 572 [8] B. SMITH, P. BJØRSTAD, AND W. GROPP, *Domain Decomposition: Parallel Multilevel Methods*  
 573 *for Elliptic Partial Differential Equations*, Cambridge University Press, Cambridge, 1996.
- 574 [9] O. E. BERG, *A lunar terminator configuration*, Earth Planet. Sci. Lett., 39 (1978), pp. 377–381.
- 575 [10] O. E. BERG, F. F. RICHARDSON, AND H. BURTON, *Apollo 17 preliminary science report*, Technical Report NASA SP-330, National Aeronautics and Space Administration, 1973.
- 576 [11] C. K. BIRDSALL AND A. B. LANGDON, *Plasma Physics via Computer Simulation (Series in*  
 577 *Plasma Physics)*, Institute of Physics Publishing, Bristol, UK, 1991.
- 578 [12] B. CAMP, T. LIN, Y. LIN, AND W. SUN, *Quadratic immersed finite element spaces and their*  
 579 *approximation capabilities*, Adv. Comput. Math., 24 (2006), pp. 81–112.
- 580 [13] H. CAO, Y. CAO, Y. CHU, X.-M. HE, AND T. LIN, *A Huygens immersed-finite-element particle-*  
 581 *in-cell method for modeling plasma-surface interactions with moving interface*, Commun.  
 582 Nonlinear Sci. Numer. Simul., 59 (2018), pp. 132–148.
- 583 [14] W. CAO, X. ZHANG, AND Z. ZHANG, *Superconvergence of immersed finite element methods for*  
 584 *interface problems*, Adv. Comput. Math., 43 (2017), pp. 795–821.
- 585 [15] Y. CAO, Y. CHU, X.-M. HE, AND T. LIN, *An iterative immersed finite element method for an*  
 586 *electric potential interface problem based on given surface electric quantity*, J. Comput.  
 587 Phys., 281 (2015), pp. 82–95.
- 588 [16] Y. CAO, Y. CHU, X. ZHANG, AND X. ZHANG, *Immersed finite element methods for unbounded*  
 589 *interface problems with periodic structures*, J. Comput. Appl. Math., 307 (2016), pp. 72–81.
- 590 [17] Y. CHU, Y. CAO, X.-M. HE, AND M. LUO, *Asymptotic boundary conditions with immersed*  
 591 *finite elements for interface magnetostatic/electrostatic field problems with open boundary*,  
 592 *Comput. Phys. Commun.*, 182 (2011), pp. 2331–2338.
- 593 [18] Y. CHU, D. HAN, Y. CAO, X.-M. HE, AND J. WANG, *An immersed-finite-element particle-in-*  
 594 *cell simulation tool for plasma surface interaction*, Int. J. Numer. Anal. Model., 14 (2017),  
 595 pp. 175–200.

[597] [19] G. L. DELZANNO AND X.-Z. TANG, *Comparison of dust charging between orbital-motion-limited*  
 598 *theory and particle-in-cell simulations*, Phys. Plasmas, 22 (2015), 113703.

[599] [20] D. DEPEW, D. HAN, J. WANG, X.-M. HE, AND T. LIN, *Immersed-Finite-Element Particle-*  
 600 *In-Cell simulations of lunar surface charging*, #199, Proceedings of the 13th Spacecraft  
 601 Charging Technology Conference, Pasadena, California, June 23-27, 2014.

[602] [21] R. E. EWING, Z. LI, T. LIN, AND Y. LIN, *The immersed finite volume element methods for the*  
 603 *elliptic interface problems. Modelling '98 (Prague)*, Math. Comput. Simulation, 50 (1999),  
 604 pp. 63–76.

[605] [22] W. FENG, X.-M. HE, Y. LIN, AND X. ZHANG, *Immersed finite element method for interface*  
 606 *problems with algebraic multigrid solver*, Commun. Comput. Phys., 15 (2014), pp. 1045–  
 607 1067.

[608] [23] J. W. FREEMAN AND M. IBRAHIM, *Lunar electric fields, surface potential and associated plasma*  
 609 *sheaths*, The Moon, 14 (1975), pp. 103–114.

[610] [24] Y. GONG, B. LI, AND Z. LI, *Immersed-interface finite-element methods for elliptic inter-*  
 611 *face problems with non-homogeneous jump conditions*, SIAM J. Numer. Anal., 46 (2008),  
 612 pp. 472–495.

[613] [25] R. GUO AND T. LIN, *A group of immersed finite-element spaces for elliptic interface problems*,  
 614 IMA J. Numer. Anal., 39 (2019), pp. 482–511.

[615] [26] R. GUO AND T. LIN, *A higher degree immersed finite element method based on a Cauchy*  
 616 *extension for elliptic interface problems*, SIAM J. Numer. Anal., 57 (2019), pp. 1545–1573.

[617] [27] R. GUO AND T. LIN, *An immersed finite element method for elliptic interface problems in three*  
 618 *dimensions*, J. Comput. Phys., 414 (2020), 109478.

[619] [28] R. GUO, T. LIN, AND Y. LIN, *Error estimates for a partially penalized immersed finite element*  
 620 *method for elasticity interface problems*, ESAIM Math. Model. Numer. Anal., 54 (2020),  
 621 pp. 1–24.

[622] [29] R. GUO, T. LIN, AND Q. ZHUANG, *Improved error estimation for the partially penalized im-*  
 623 *mersed finite element methods for elliptic interface problems*, Int. J. Numer. Anal. Mod.,  
 624 16 (2019), pp. 575–589.

[625] [30] R. GUO AND X. ZHANG, *Solving Three-Dimensional Interface Problems with Immersed Finite*  
 626 *Elements: A-Priori Error Analysis*, preprint, arXiv:2004.08984, 2020.

[627] [31] J. GUZMÁN, M. A. SÁNCHEZ, AND M. SARKIS, *Higher-order finite element methods for elliptic*  
 628 *problems with interfaces*, ESAIM Math. Model. Numer. Anal., 50 (2016), pp. 1561–1583.

[629] [32] J. S. HALEKAS, G. T. DELORY, D. A. BRAIN, R. P. LIN, M. O. FILLINGIM, C. O. LEE, R. A.  
 630 MEWALDT, T. J. STUBBS, W. M. FARRELL, AND M. K. HUDSON, *Extreme lunar surface*  
 631 *charging during solar energetic particle events*, Geophys. Res. Lett., 34 (2007), L02111.

[632] [33] J. S. HALEKAS, G. T. DELORY, R. P. LIN, T. J. STUBBS, AND W. M. FARRELL, *Lunar prospector*  
 633 *observations of the electrostatic potential of the lunar surface and its response to incident*  
 634 *currents*, J. Geophys. Res., 113 (2008), A09102.

[635] [34] J. S. HALEKAS, Y. SAITO, G. T. DELORY, AND W. M. FARRELL, *New views of the lunar plasma*  
 636 *environment*, Planet. Space Sci., 59 (2011), pp. 1681–1694.

[637] [35] D. HAN, *Particle-in-Cell Simulations of Plasma Interactions with Asteroidal and Lunar Sur-*  
 638 *faces*, PhD thesis, University of Southern California, 2015.

[639] [36] D. HAN AND J. WANG, *3-D fully-kinetic particle-in-cell simulations of small asteroid charging*  
 640 *in the solar wind*, IEEE Trans. Plasma Sci., 47 (2019), pp. 3682–3688.

[641] [37] D. HAN, J. WANG, AND X.-M. HE, *PIFE-PIC: A 3-D parallel immersed finite element particle-*  
 642 *in-cell framework for plasma simulations*, #AIAA-2018-2196, Proceeding of 2018 AIAA  
 643 Aerospace Sciences Meeting, Kissimmee, Florida, January 8-12, 2018.

[644] [38] D. HAN, J. WANG, AND X.-M. HE, *A non-homogeneous immersed-finite-element particle-in-*  
 645 *cell method for modeling dielectric surface charging in plasmas*, IEEE Trans. Plasma Sci.,  
 646 44 (2016), pp. 1326–1332.

[647] [39] D. HAN, J. WANG, AND X.-M. HE, *Immersed-finite-element particle-in-cell simulations of*  
 648 *plasma charging at lunar terminator*, J. Spacecraft Rockets, 55 (2018), pp. 1490–1497.

[649] [40] D. HAN, P. WANG, X.-M. HE, T. LIN, AND J. WANG, *A 3D immersed finite element method*  
 650 *with non-homogeneous interface flux jump for applications in particle-in-cell simulations*  
 651 *of plasma-lunar surface interactions*, J. Comput. Phys., 321 (2016), pp. 965–980.

[652] [41] C. HE AND X. ZHANG, *Residual-based a posteriori error estimation for immersed finite element*  
 653 *methods*, J. Sci. Comput., 81 (2019), pp. 2051–2079.

[654] [42] X.-M. HE, *Bilinear immersed finite elements for interface problems*, Ph.D. Dissertation, Vir-  
 655 *ginia Polytechnic Institute and State University, (2009).*

[656] [43] X.-M. HE, T. LIN, AND Y. LIN, *Approximation capability of a bilinear immersed finite element*  
 657 *space*, Numer. Methods Partial Differential Equations, 24 (2008), pp. 1265–1300.

[658] [44] X.-M. HE, T. LIN, AND Y. LIN, *A bilinear immersed finite volume element method for the*  
 659 *diffusion equation with discontinuous coefficients, dedicated to Richard E. Ewing on the*  
 660 *occasion of his 60th birthday*, Commun. Comput. Phys., 6 (2009), pp. 185–202.

[45] X.-M. HE, T. LIN, AND Y. LIN, *Interior penalty bilinear IFE discontinuous Galerkin methods for elliptic equations with discontinuous coefficient, dedicated to David Russell's 70th birthday*, J. Syst. Sci. Complex., 23 (2010), pp. 467–483.

[46] X.-M. HE, T. LIN, AND Y. LIN, *Immersed finite element methods for elliptic interface problems with non-homogeneous jump conditions*, Int. J. Numer. Anal. Model., 8 (2011), pp. 284–301.

[47] X.-M. HE, T. LIN, AND Y. LIN, *The convergence of the bilinear and linear immersed finite element solutions to interface problems*, Numer. Methods Partial Differential Equations, 28 (2012), pp. 312–330.

[48] X.-M. HE, T. LIN, AND Y. LIN, *A selective immersed discontinuous Galerkin method for elliptic interface problems*, Math. Methods Appl. Sci., 37 (2014), pp. 983–1002.

[49] X.-M. HE, T. LIN, Y. LIN, AND X. ZHANG, *Immersed finite element methods for parabolic equations with moving interface*, Numer. Methods Partial Differential Equations, 29 (2013), pp. 619–646.

[50] G. H. HEIKEN, D. T. VANIMAN, AND B. M. FRENCH, *Lunar Sourcebook: A User's Guide to the Moon*, Cambridge University Press, Cambridge, 1991.

[51] R. W. HOCKNEY AND J. W. EASTWOOD, *Computer Simulation Using Particles*, Adam Hilger, London, 1988.

[52] J. D. JACKSON, *Classical electrodynamics*, 3rd ed., Wiley, New York, 1999.

[53] H. JIAN, Y. CHU, H. CAO, Y. CAO, X.-M. HE, AND G. XIA, *Three-dimensional IFE-PIC numerical simulation of background pressure's effect on accelerator grid impingement current for ion optics*, Vacuum, 116 (2015), pp. 130–138.

[54] R. KAFAFY, T. LIN, Y. LIN, AND J. WANG, *Three-dimensional immersed finite element methods for electric field simulation in composite materials*, Int. J. Numer. Meth. Engrg., 64 (2005), pp. 940–972.

[55] R. KAFAFY AND J. WANG, *Whole subscale ion optics simulation: Direct ion impingement and electron backstreaming*, in 41st AIAA/ASME/SAE/ASEE Joint Propulsion Conference and Exhibit, AIAA 2005-3691, Tucson, Arizona, July 2005.

[56] R. KAFAFY AND J. WANG, *Whole ion optics gridlet simulations using a hybrid-grid immersed-finite-element particle-in-cell code*, J. Propul. Power, 23 (2007), pp. 59–68.

[57] R. I. KAFAFY AND J. WANG, *A hybrid grid immersed finite element particle-in-cell algorithm for modeling spacecraft-plasma interactions*, IEEE Trans. Plasma Sci., 34 (2006), pp. 2114–2124.

[58] D. KWAK, S. JIN, AND D. KYEONG, *A stabilized P1-nonconforming immersed finite element method for the interface elasticity problems*, ESAIM Math. Model. Numer. Anal., 51 (2017), pp. 187–207.

[59] Z. LI, *The immersed interface method using a finite element formulation*, Appl. Numer. Math., 27 (1998), pp. 253–267.

[60] Z. LI, T. LIN, Y. LIN, AND R. C. ROGERS, *An immersed finite element space and its approximation capability*, Numer. Methods Partial Differential Equations, 20 (2004), pp. 338–367.

[61] Z. LI, T. LIN, AND X. WU, *New Cartesian grid methods for interface problems using the finite element formulation*, Numer. Math., 96 (2003), pp. 61–98.

[62] T. LIN, Y. LIN, AND X. ZHANG, *Partially penalized immersed finite element methods for elliptic interface problems*, SIAM J. Numer. Anal., 53 (2015), pp. 1121–1144.

[63] T. LIN, D. SHEEN, AND X. ZHANG, *A locking-free immersed finite element method for planar elasticity interface problems*, J. Comput. Phys., 247 (2013), pp. 228–247.

[64] T. LIN, D. SHEEN, AND X. ZHANG, *A nonconforming immersed finite element method for elliptic interface problems*, J. Sci. Comput., 79 (2019), pp. 442–463.

[65] T. LIN, Q. YANG, AND X. ZHANG, *A priori error estimates for some discontinuous Galerkin immersed finite element methods*, J. Sci. Comput., 65 (2015), pp. 875–894.

[66] C. LU, J. WAN, Y. CAO, AND X.-M. HE, *A fully decoupled iterative method with three-dimensional anisotropic immersed finite elements for Kaufman-type discharge problems*, Comput. Meth. Appl. Mech. Eng., 372 (2020), 113345.

[67] C. LU, Z. YANG, J. BAI, Y. CAO, AND X.-M. HE, *Three-dimensional immersed finite element method for anisotropic magnetostatic/electrostatic interface problems with non-homogeneous flux jump*, Int. J. Numer. Meth. Eng., 121 (2020), pp. 2107–2127.

[68] D. LUND, J. ZHAO, A. LAMB, AND D. HAN, *Fully Kinetic PIFE-PIC Simulations of Plasma Charging at Lunar Craters*, in AIAA SciTech 2020, AIAA 2020-1549, Orlando, Florida, January 6–10, 2020.

[69] D. S. MCKAY, G. HEIKEN, A. BASU, G. BLANFORD, S. SIMON, R. REEDY, B. M. FRENCH, AND J. PAPIKE, *Chapter 7: The lunar regolith*, in *Lunar Sourcebook: A User's Guide to the Moon*, Cambridge University Press, Cambridge, 1991, pp. 285–356.

[70] NASA-JPL, *Moon Trek*, trek, nasa.gov/moon (15 July 2020).

[71] A. R. POPPE, M. PIQUETTE, A. LIKHANSKII, AND M. HORÁNYI, *The effect of surface topography on the lunar photoelectron sheath and electrostatic dust transport*, Icarus, 221 (2012), pp. 135–146.

[72] T. PREUSSER, M. RUMPF, S. SAUTER, AND L. O. SCHWEN, *3D composite finite elements for elliptic boundary value problems with discontinuous coefficients*, SIAM J. Sci. Comput., 33 (2011), pp. 2115–2143.

[73] D. L. REASONER AND W. J. BURKE, *Characteristics of the lunar photoelectron layer in the geomagnetic tail*, J. Geophys. Res., 77 (1972), pp. 6671–6687.

[74] Y. G. SHKURATOV AND N. V. BONDARENKO, *Regolith layer thickness mapping of the moon by radar and optical data*, Icarus, 149 (2001), pp. 329–338.

[75] T. J. STUBBS, J. S. HALEKAS, W. M. FARRELL, AND R. R. VONDRAK, *Lunar surface charging: A global perspective using lunar prospector data*, in Workshop on Dust in Planetary Systems (ESA SP-643), H. Krueger and A. Graps, eds., Kauai, Hawaii, USA, September 26-30, 2005, pp. 181–184.

[76] X.-Z. TANG AND G. L. DELZANNO, *Orbital-motion-limited theory of dust charging and plasma response*, Phys. Plasmas, 21 (2014), p. 123708.

[77] D. HAN AND J. WANG, *Simulations of Ion Thruster Plume Contamination with A Whole Grid Sputtered Mo Source Model*, in 49th AIAA/ASME/SAE/ASEE Joint Propulsion Conference and Exhibit, AIAA 2013-3888, San Jose, California, July 14 - 17, 2013.

[78] S. VALLAGHÈ AND T. PAPADOPOULO, *A trilinear immersed finite element method for solving the electroencephalography forward problem*, SIAM J. Sci. Comput., 32 (2010), pp. 2379–2394.

[79] C. WANG, P. SUN, AND Z. LI, *An iterative approach for constructing immersed finite element spaces and applications to interface problems*, Int. J. Numer. Anal. Model., 16 (2019), pp. 167–191.

[80] J. WANG, Y. CAO, R. KAFAFY, J. PIERRU, AND V. K. DECYK, *Simulations of ion thruster plume-spacecraft interactions on parallel supercomputer*, IEEE Trans. Plasma Sci., 34 (2006), pp. 2148–2158.

[81] J. WANG, X.-M. HE, AND Y. CAO, *Modeling spacecraft charging and charged dust particle interactions on lunar surface*, in Proceedings of the 10th Spacecraft Charging Technology Conference, Biarritz, France, 2007.

[82] J. WANG, X.-M. HE, AND Y. CAO, *Modeling electrostatic levitation of dusts on lunar surface*, IEEE Trans. Plasma Sci., 36 (2008), pp. 2459–2466.

[83] R. WILLIS, M. ANDERECK, B. FEUERBACHER, AND B. FITTON, *Photoemission and secondary electron emission from lunar surface material*, in Photon and Particle Interactions with Surfaces in Space, R. Grard, ed., Astrophysics and Space Science Library 37, Springer, Amsterdam, 1973.

[84] W. YU, D. HAN, AND J. WANG, *Numerical Simulations of Dust Dynamics Around Small Asteroids*, IEEE Trans. Plasma Sci., 47 (2019), pp. 3724–3730.

[85] W. YU, J. J. WANG, AND D. HAN, *Numerical Modeling of Dust Dynamics Around Small Asteroids*, in AIAA SPACE Forum 2016, AIAA 2016-5447, Long Beach, California, September 13-16, 2016.

[86] H. ZHANG, T. LIN, AND Y. LIN, *Linear and quadratic immersed finite element methods for the multi-layer porous wall model for coronary drug-eluting stents*, Int. J. Numer. Anal. Mod., 15 (2018), pp. 48–73.

[87] Q. ZHANG, K. ITO, Z. LI, AND Z. ZHANG, *Immersed finite elements for optimal control problems of elliptic PDEs with interfaces*, J. Comput. Phys., 298 (2015), pp. 305–319.

[88] X. ZHANG, *Nonconforming immersed finite element methods for interface problems*, Ph.D. Dissertation, Virginia Polytechnic Institute and State University, 2013.